DRAFT VERSION MAY 11, 2016
Preprint typeset using LaTeX style emulateapj v. 01/23/15

A CONSTANT RATIO BETWEEN BLACK HOLE ACCRETION AND STAR FORMATION RATE IN IR-BRIGHT AGNS

Y. SOPHIA DAI (戴昱)[1], BELINDA J. WILKES[2], JACQUELINE BERGERON[3,4], ALAIN OMONT[3,4], JOANNA KURASZKIEWICZ[2], ADAM ATANAS[5], AND HARRY I. TEPLITZ[1]

Draft version May 11, 2016

ABSTRACT

We study the relationship between the X-ray luminosity and star formation rate (SFR) in a sample of far-infrared(FIR)-detected active galactic nuclei (AGNs). This IR-bright AGN sample consists of 828 objects in $0.2< z < 2.5$, and spans four orders of magnitude in $L_X = 10^{42\sim46}$erg s^{-1}. We calculated the SFR from the AGN-removed IR luminosity based on spectral energy distribution (SED) fitting. We observe a strong correlation between L_{AGN} and SFR, after removing the redshift effect. We notice that binning the sample by SFR instead of L_{AGN} results in a stronger correlation, consistent with the shorter timescale and larger amplitude for AGN variability than star formation. The AGN's Eddington ratios and SMBH masses do not have a significant effect on the correlation. We find a constant ratio between the SFR and the black hole accretion rate (BHAR) regardless of redshift or SMBH mass around log(SFR/BHAR)$= 2.82 \pm 0.04$, with a scatter of 0.57. Inclusion of $z < 0.2$ and $z > 2.5$ IR-bright AGNs yields consistent flat slopes, indicating little to no redshift effect. This constant mass accretion ratio coincides with the accumulated mass ratio between SMBH and host stellar mass in the local universe. Our results support the secular evolution picture, where the SMBH are growing at a relatively constant rate with the host galaxy, possibly from a common gas supply,regardless of the level of accretion activity or the mass of the SMBH.

Subject headings: galaxies: active — galaxies: star formation — infrared: galaxies — X-rays: galaxies

1. INTRODUCTION

One of the outstanding questions in galaxy formation and evolution is how the central engine of a galaxy, the supermassive black hole (SMBH), interacts with and influences the host galaxy. A general connection has been confirmed by several empirical correlations between the SMBH mass ($M_\bullet$) and the luminosity, mass, and stellar velocity dispersion of the host, both locally and at high redshifts (e.g. Kormendy & Richstone 1995; Ferrarese & Merritt 2000; Merloni et al. 2003). A constant ratio has been found between $M_\bullet$ and the bulge mass (M_{bulge}), confirmed by several studies to be $\log(M_{\rm bulge}/M_\bullet) \sim 2.9\pm0.5$ (Magorrian et al. 1998; Merritt & Ferrarese 2001; McLure & Dunlop 2002; Marconi & Hunt 2003), or $\log(M_{\rm bulge}/M_\bullet) \sim 2.3\pm0.3$, after correcting the $M_\bullet$ values by galaxy types (Kormendy & Ho 2013). Despite tremendous progress on the demographic studies of SMBHs, it is still under debate whether, and if so, how the SMBH regulates the host galaxy formation. Different scenarios, sometimes resulting in opposite predictions, exist. For instance, theories and simulations have suggested that active BH accretion will suppress and eventually shut down star formation by heating or expelling the cold gas in the host, via a process of 'feedback' (e.g. Silk & Rees 1998; Di Matteo et al. 2005; Bower et al. 2006; Hopkins et al. 2006; Debuhr et al. 2012). At the same time, competing theories of in tandem BH and galaxy growth, via accretion and star formation, are also prevalent (e.g. Springel et al. 2005). The latter is supported locally by the tight correlations between the black hole and galaxy spheroid mass (Kormendy & Ho 2013), the cosmic evolution of total star formation rate (SFR) and BH accretion rates (BHARs) up to $z = 3$ (Silverman et al. 2008; Madau & Dickinson 2014), and by the cold flow model of inflowing cosmological cold gas supplies, especially for the high z universe (e.g. Bournaud et al. 2011).

Recent studies have tried to directly trace the global properties of AGNs and the host galaxies via correlations between BHAR or AGN luminosities traced by X-ray luminosities (L_X) and SFR or IR luminosities. Given the differences in spatial scales between AGN ($\sim$100 pc) and star formation (up to tens of kpc), any observed correlation would indicate intrinsic connections (Alexander & Hickox 2012; Kormendy & Ho 2013). Different correlations (or lack of) have been inferred by different groups. Earlier results based on X-ray and sub-mm observations have found a significant correlation between L_X and SFR (or L_{FIR}) at $L_X > 10^{44}$erg s^{-1} for $z \sim 1$ AGNs, but no evidence of correlation at lower z or lower luminosities (Lutz et al. 2010). Later studies using X-ray and *Herschel* observations confirmed and expanded these results. Using *Herschel* PACS data, Shao et al. (2010) noticed little dependence of L_{FIR} on L_X at $z > 1$ and $L_X < 10^{44}$erg s^{-1}, and strongly correlated L_X and SFR locally and in luminous AGNs. Similarly, several studies have confirmed these two-fold relations based on X-ray selected AGNs with PACS detection and stacks: a positive correlation between L_X and the specific SFR (sSFR, SFR over stellar mass) at $L_X > 10^{43}$erg s^{-1} and $z > 1$, but no correlation at lower redshifts or lower luminosities (Rovilos et al. 2012); overall uncorrelated L_X and far-IR luminosities ($L_{60\mu m}$) at $0 < z < 2.5$, but an enhanced SFR at $L_X > 10^{45}$erg s^{-1} at $z < 1$ (Rosario et al. 2012); an overall lack of SFR enhancement in AGN hosts at $0.3 < z < 2.1$ in optically selected broad-line AGNs (quasars, Rosario et al. 2013b), and in X-

[1] Caltech-Infrared Processing and Analysis Center, 1200 East California Boulevard, Pasadena, CA 91125, USA; ydai@caltech.edu
[2] Harvard-Smithsonian Center for Astrophysics, 60 Garden Street, Cambridge, MA 02138, USA
[3] CNRS, UMR7095, Institut d'Astrophysique de Paris, F-75014, Paris, France
[4] UPMC Univ Paris 06, UMR7095, Institut d'Astrophysique de Paris, F-75014, Paris, France
[5] Harvard University, 60 Garden Street, Cambridge, MA 02138, USA

ray selected AGNs at $10^{42} < L_X < 10^{44}$erg s^{-1} from $0 < z < 3$ (Mullaney et al. 2012a). A strong SFR decrease in powerful AGNs and X-ray quasars was found by Page et al. (2012) and interpreted as AGN feedback that suppresses star formation in the host. Analysis of a larger sample showed that this result was related to limited sample size and cosmic variance (Harrison et al. 2012) and that the mean SFRs were constant over a broad range of X-ray luminosities. Recent studies have also found suppressed star formation in X-ray selected quasars (Barger et al. 2015) **and in $z < 0.05$ Seyfert galaxies and LINERs (Shimizu et al. 2015).** Common interpretations of these phenomena yield two different mechanisms at high and low AGN luminosities. Major mergers dominate the luminous end, triggering simultaneous BH accretion and starburst episodes. Secular evolution is responsible for the majority of galaxies with moderate nuclear activity, where non-merger driven star formation is happening in step with the SMBH accretion, possibly fueled by the same gas reservoir (e.g. Shao et al. 2010; Mullaney et al. 2012b). Evidence of such coeval formation has also been found in massive galaxies regardless of the level of SMBH accretion (Podigachoski et al. 2015).

Studies of various galaxy populations have found AGNs lying mostly along the star formation galaxies main sequence (MS, e.g. Noeske et al. 2007; Elbaz et al. 2007, 2011; Pannella et al. 2009; Rodighiero et al. 2011), **with AGNs residing mainly in MS hosts exhibiting similar SFR and stellar mass to inactive star forming galaxies, or showing enhanced average SFR only in a small fraction ($<$10%) of, or for a short period of time among AGN hosts (e.g. Santini et al. 2012; Mullaney et al. 2012a; Rovilos et al. 2012; Rosario et al. 2013a,b)**. Moreover, positive correlations have been found between the L_X or BHARs and SFR regardless of AGN luminosity (e.g. Symeonidis et al. 2011; Rovilos et al. 2012; Chen et al. 2013, 2015), and between L_{AGN} and circumnuclear SFR in local Seyfert galaxies (Diamond-Stanic & Rieke 2012). Recently, Matsuoka & Woo (2015) investigated a large sample of optically selected type 2 AGNs at $z < 0.22$ and also found a positive linear correlation between infrared luminosity (L_{IR}) based on *AKARI* or *Herschel* photometry and L_{AGN} based on emission lines. A positive correlation suggests two possible scenarios of AGN/SF coevolution: either a strong cold gas inflow is fueling the black hole accretion and galaxy star formation simultaneously, or a merger-triggered nuclear starburst with strong accretion occurs during the early encounter (Hopkins 2012).

At first glance, the inconsistent, sometimes contradictory results are confusing. Nevertheless, these differences may arise from the different selection criteria for the various samples and different methods of analysis. For instance, studies comparing SFR with observed instantaneous L_X could result in different conclusions from those using average L_X. A flat or non-correlation may become significant and positive if average instead of instant L_X is used (Azadi et al. 2015), while the inclusion of upper limits seems to flatten the observed trend (e.g. Stanley et al. 2015). Other factors that could mask a real correlation between AGN and SF properties include: the AGN evolutionary stages, be it before, during, or after the merging process; the shorter variabilities of AGNs as compared to SFR, and the different Eddington ratio (ER) distributions (Hickox et al. 2014; Volonteri et al. 2015b; Stanley et al. 2015). The different observed correlations may also arise from the different ways of projecting the sample: L_X and SFR are not as strongly correlated when binned by AGN luminosity or BHAR then binned by SFR—a result that can be explained by the shorter timescales of AGN variability (e.g. Hickox et al. 2014; Chen et al. 2015; Volonteri et al. 2015a). On the other hand, the way of measuring SFRs could also introduce systematics. Earlier studies depended on monochromatic luminosities, usually single-band *Hershcel* PACS or SPIRE photometry, to estimate the SFR, whereas more evidence has shown that the AGN emission could extend to rest-frame $\lambda > 50\mu$m and significantly alter the intrinsic far-IR SED (e.g. Dai et al. 2012). It is necessary to carry out careful SED-based AGN/SF decomposition to achieve a reliable SFR estimate.

The aim of this paper is to test the above scenarios using a statistically significant sample of IR-bright AGNs detected in both X-ray and FIR, and with known redshifts. This sample is selected from the 11 deg^2 X-ray Multi-Mirror Mission (XMM)-Newton Large Scale Structure (XMM-LSS) field. In Section 2, we describe the multi-wavelength data and the AGN selection; In Section 3 we calculate the L_{IR}, SFR, SMBH mass, and Eddington ratios; We then summarize and discuss our results in Section 4 followed by a summary (Section. 5). In this work, we assume a concordance cosmology with H_0=70 km s^{-1} Mpc^{-1}, Ω_M=0.3, and Ω_Λ=0.7.

2. THE SAMPLE

We selected a sample consisting only of AGNs detected in both X-ray and FIR, with redshifts and multi-wavelength photometry for SED and luminosity estimates.

We started with the 10 ks XMM-LSS X-ray deep full exposure catalog (XLSSd, Pierre et al. 2007; Chiappetti et al. 2013, C13). The flux limits (50% detection probability) are 3×10^{-15} erg s^{-1}(0.5-2 keV) and 1×10^{-14} erg s^{-1}(2-10 keV) over nominal survey pointing. **We restricted our sample to the 2,399 objects with redshift information, which consists of 75% of the total 3,194 hard X-ray detected objects in the field. The remaining 795 objects have no z estimate due to the non-uniform multi-wavelength coverage of the field. We did not limit our sample to point-sources,** as extended morphologies have also been reported to be common in IR-detected quasars (Dai et al. 2014). For 50% (1,190) of the hard X-ray targets, spectroscopic redshifts (spec-z) are available from a. the SDSS-BOSS DR12[6] catalog (943, within a matching radius of 6″); b. various publications (229[7], for detailed list of reference see Melnyk et al. (2013), M13); c. an MMT-Hectospec redshift survey based on 24μm priors (18, a similar survey is described in detail in Dai et al. (2014)). In parenthesis are the numbers of unique spectra in these catalogs. For the 301 objects with both BOSS and M13 spectra, the redshifts are consistent in $>$97% cases, and the spec-z from BOSS was used. The remaining 50% (1,209 objects, excluding the ones with spec-z) have photometric redshifts (photo-z) from the XMM-LSS photo-z catalog (M13), which used the identical XMM X-ray catalog as the prior.

We then matched the 2,399 hard X-ray targets to the HerMES DR3 and DR2 catalogs[8] (Roseboom et al. 2010, 2012; Oliver et al. 2012; Wang et al. 2014) and identified 929 AGNs with both hard X-ray (2-10 keV) and 250 μm ($> 3\sigma$) detections. The HerMES XMM-LSS SWIRE field covers

[6] http://skyserver.sdss.org/dr12
[7] not counting the 301 objects with SDSS spectra
[8] http://hedam.lam.fr/HerMES/

18.87 deg^2 and has a sensitivity of 6.6 mJy (3σ) at 250μm (Wang et al. 2014). A matching radius of 10″, between the 6″ PSF for XMM and the 18″ PSF for Herschel-SPIRE1, was chosen to maximize the matching counts while minimizing random associations. The **rest frame** hard band X-ray luminosity (derived from 2-10 keV, hereafter referred to as L_X) was determined assuming a photon index of Gamma=1.7 and $N_H(Gal) = 2.6e20\,cm^{-2}$ (C13). We **corrected L_X for intrinsic obscuration** based on redshift and the observed hardness ratio (HR), with HR = (H − S)/(H + S), where H and S are the count rates in the hard (2-10 keV) and soft (0.5-2 keV) bands, respectively. **We applied a simple correction for Galactic and intrinsic obscuration to the rest frame L_X. We first determined the intrinsic neutral hydrogen column density (N_H) based on the HR and z of each source using the PIMMS tool[9], assuming the spectral form described above, and then applied the corresponding obscuration correction to the observed X-ray flux where possible. We did not correct for sources with HR < -0.5 as their spectra are softer than the assumed spectrum. For the 139 sources undetected in the soft band, no upper limits for the soft-band X-ray counts were available, so we adopted the observed X-ray flux as a lower limit for these obscured sources. These lower limits are treated as detections in the analysis and their impact on the observed relation will be discussed in Sec. 4.** Table 1 summarizes the redshift and luminosity distributions of our sample. The absorption corrected L_X are listed in Table 2. The method used to calculate the IR luminosity will be described in Section.3.

In this study, we focused on the 828 far-IR detected X-ray AGNs with $L_X \geq 10^{42}$ erg s^{-1} and at $0.2 < z < 2.5$ (main sample). A total of 34 objects with $L_X < 10^{42}$erg s^{-1} were rejected. Out of statistical concerns, from the with $L_X \geq 10^{42}$erg s^{-1} objects, we also removed 36 $z < 0.2$ objects and 31 $2.5 < z < 4.2$ objects from the final sample. We will use these low and high z targets as a supplementary sample for comparison in the discussion section. Because of the requirement of IR detection, hereafter we will refer to this main sample as IR-bright AGNs. Since not all AGNs are active in the IR with high dust mass and SFR (see Sec. 3.1), on an average basis, the IR-bright AGNs are found during a stronger star formation phase than their IR-undetected counterparts with comparable L_X. Among the IR-undetected AGNs, a fraction of them will be the 'normal', dust-expelled AGNs with limited star formation (e.g. $L_{IR,SF} < 43$ erg s^{-1}). These non-star forming AGNs would be referred to as 'IR-quiescent' AGNs in the following sections. The L_X in this sample ranges from $10^{42.0}$ to $10^{45.6}$ erg s^{-1}, with a median of $10^{44.1}$erg s^{-1}. About 61% of the sample has an HR < -0.2 (X-ray unobscured, e.g. Szokoly et al. 2004). In the spec-z subsample, 57% show broad emission lines (optical type 1). Combining these two samples we found that overall 66% of the sample is unobscured.

The sample of 828 X-ray selected IR-bright AGNs spans a redshift range of $0.2 < z < 2.5$, with a median and mean of $z = 1.07$ and 1.14, respectively. About half (467, 56%) of the sample have an $L_X \geq 10^{44}$erg s^{-1}; and the rest (361, 44%) are at $10^{42} \leq L_X < 10^{44}$erg s^{-1}, confirming their AGN nature. About 60% of the sample (483) have spec-z (383 from BOSS, 38 from MMT, and 62 from M13), and the remaining 345 objects have photo-z from M13. The multi-wavelength data associated with the X-ray sources were adopted from the 2XLSSdOPT catalog from C13. A matching radius of 6″ (PSF for XMM) was used between the X-ray catalogs and the GALEX, CFHTLS, SWIRE (Lonsdale et al. 2003), and UKIDSS catalogs. A detailed description of the matching of X-ray sources to their counterparts can be found in C13.

[9] http://cxc.harvard.edu/toolkit/pimms.jsp

2.1. **Selection Effects**

Figure 1 plots the z and luminosity distribution of the IR-bright AGN sample, color coded by their rest-frame L_X. Since the sample is flux-limited, the IR-bright AGNs are unavoidably affected by the Malmquist bias, especially in regions with no overlap between different colors. The IR-bright AGNs share similar L_X luminosity distribution with the parent sample (Figure. 1, inset), indicating an intrinsic L_X distribution of the hard X-ray targets regardless of their FIR activeness. This is consistent with other results (e.g. 3C samples, Podigachoski et al. 2015), where the far-IR detection rate is also unrelated to the radio source type (i.e. orientation). The redshift distribution, on the other hand, shows a higher fraction of IR-bright AGNs at $0.2 < z < 0.6$ than the parent sample. This is due to the requirements of both far-IR detection and available redshift estimates based on the optical data. As a result of the latter, at higher z, fainter objects fall below the flux limits, and will not be detected. Since the low z targets are dominated by type 2 sources and more affected by obscuration, and at the high z, the source numbers are low, we decided to focus on the intermediate redshift range of $0.2 < z < 2.5$.

It is clear that the z∼2 sample is systematically ∼2-3 dex more luminous than the z<0.5 objects. This increase in L_X is consistent with the evolution of L* in the AGN luminosity function (e.g. Croom et al. 2009; Ranalli et al. 2015), indicating that we are sampling the same portion of the AGN luminosity function throughout the redshift range. This is also true for the SFR indicator $L_{IR,SF}$, as the SFR density also increases by 1-1.5 dex from $z = 0$ to $z = 2$, comparable to the luminosity increase in Figure. 1.

Finally, the z requirement introduces another selection effect to the sample, since both spec-z and photo-z determination require optical spectra or photometry. As a result, the Eddington ratio (ER) distribution is not homogeneous across redshift but is biased against low ER, less luminous targets, especially at high z. We will discuss this selection effect in more detail in Section. 3.2. These selection effects must be kept in mind when interpreting the results in Sec. 4.

3. ANALYSIS

3.1. *IR luminosity, SFR, and Dust mass*

We estimated the total IR and far-IR luminosities (L_{IR}^{8-1000}, $L_{FIR}^{30-1000}$) based on the rest-frame SEDs for the IR-bright AGNs. The SEDs are constructed from optical to the FIR bands: u*, g',r',i',z' (CFHTLS); J, H, K (UKIDSS); 3.6, 4.5, 5.8, 8.0 μm (SWIRE-IRAC); 24, 70, 160 μm (SWIRE-MIPS); 250, 350, 500 μm (HerMES). **For the Herschel data, total errors (including confusion noise) were used in the fitting procedure.** We adopted the $T - \alpha - \beta$ model from Blain et al. (2003), where T is the dust temperature, β is the emissivity index, and α the power-law index. This method fits the SED longwards of 5μm without any presumptions of the heating source, be it AGN or star formation. Instead of a pure modified blackbody (MBB) on both the Rayleigh-Jeans and Wien tails, a power-law function ($f_\nu \propto \nu^{-\alpha} B(\nu, T_{dust})$) was

used in the mid-IR (5-10 μm) Wien side to account for contributions from warmer dust. Here $B(\nu, T_{\rm dust})$ is the blackbody Planck function. We adopted $\beta = 2.0$ (Priddey et al. 2003) and allow α to vary. This additional term is then matched to the MBB component at a transition point, where the two functions have equal zeroth and first order derivatives. The transition wavelengths vary from case to case. The corresponding peak dust temperature ranges from 5 to 100 K, with a median around 30K.

Utilizing the X-ray data, we developed a 3-step method to decompose the AGN and star formation contributions in the FIR regime. Step 1 is to estimate the AGN contributed IR luminosity from the X-ray luminosity. This correlation is based on the assumption that the X-ray, especially in the hard band, and mid-IR are both dominated by AGN emission. Here we chose 6 μm to enable extrapolation into the far-IR regime because AGN SEDs may vary significantly longwards of the rest frame 10 μm for different AGN populations. For instance, in Dai et al. (2012) we found a variation on the order of 1.5 dex between IR-detected and IR-undetected AGNs. Several published relations exist regarding the X-ray to 6 μm correlations for AGNs with L_X in the range of 10^{41-46} erg s^{-1}, for both obscured and unobscured populations (e.g. Lutz et al. 2004; Gandhi et al. 2009; Fiore et al. 2009; Lanzuisi et al. 2009; Mateos et al. 2015; Stern 2015). In this work we adopted the recent results from Stern (2015): $\log L(2-10\,{\rm keV}) = 40.981 + 1.024x - 0.047x^2$, where $L(2-10\,{\rm keV})$ is in units of erg s^{-1}, and x=log($\nu L_\nu(6\mu m)/10^{41}$erg s^{-1}). This relation is consistent with earlier work at the fainter end and extends to the $L_X > 10^{45}$ erg s^{-1} regime that is covered by this sample.

In step 2, we converted the X-ray based 6 μm luminosity (L_6) to the AGN IR ($L_{IR,AGN}$) and bolometric luminosities (L_{AGN}) using an AGN template that extends to rest-frame 1000 μm (Dai et al. 2012, D12). The D12 mean SED template was chosen because it was constructed with detailed FIR SED information with SPIRE detections and stacks[10], while earlier work, e.g. Richards et al. (2006, R06) extrapolated beyond rest-frame 95 μm as no data were available at the time. Since the AGN contribution to the rest-frame FIR is an unsettled question, in this study we adopted the mean SED based on the stacks of $\sim$300 SPIRE-undetected quasars. This is likely an underestimate for the small subsample of AGN-starbursts ($\sim$10% of all quasars according to D12). Compared to the extrapolation of the R06 template, the D12 conversion factors are $<$0.1 dex and $<$0.2 dex lower between 6 μm luminosity and total IR and FIR luminosities. These differences are 10 times smaller than the intrinsic scatter of a few dex in both templates and can be considered consistent. In summary, factors of 1.0 and 2.5 were used to convert $L_{6,AGN}$ to $L_{FIR,AGN}$ and $L_{IR,AGN}$, respectively; and a factor of 8.0 was used to convert the L_X based L_6 to the AGN bolometric luminosity L_{AGN}. **Combining the flux error, SED fitting error, and the intrinsic uncertainty of the conversions, a typical error of L_{AGN} is $\geq$30%.**

In the last step (step 3), we subtracted $L_{IR,AGN}$ from the observed L_{IR} derived from SED fitting, and estimated the SFR based on the AGN-corrected $L_{IR,SF}$ using the Kennicutt relation (Kennicutt 1998)[11]. The average AGN contribution to the total IR luminosity is $\sim$47%, while 20% of the sample has an AGN dominated ($>$50%) L_{IR}. The corrected SFR decreases by 50% or more for $\sim$20% of the IR-bright AGNs. **As a result of the scatter in the $L_X - L_{6,AGN}$ relation, the uncertainties in $L_{IR,SF}$ and SFR are also higher for objects with an AGN-dominant IR.** The high correction factor values demonstrate the importance of AGN/SF decomposition for SFR estimates. On the other hand, the AGN contribution to the FIR luminosity is significantly lower, with an average value of 24%. Only 8% of the sample has an AGN dominated FIR. The corrected SFR based on L_{FIR} dropped by an average of 10% after removing the AGN contribution in the FIR region (30–1000 μm). We compared the AGN-removed $L_{IR,SF}$ to the total L_{FIR} and found that they are consistent for $>$80% of the sources. Therefore we suggest that when AGN decomposition is not possible, $L_{FIR}(30-1000)$ can be used as a convenient proxy for the AGN removed $L_{IR,SF}$. As a check, we subtracted the average contribution to L_X from star formation using the SFR-L_X relation (Ranalli et al. 2003), and confirmed that L_X is dominated by the AGN: the non-AGN contribution to L_X is $<$2% in all chosen redshift and luminosity bins.

We then estimated the dust mass ($M_{\rm dust}$) of the sample using the following formula (e.g. Beelen et al. 2006):

$$M_{\rm dust} = \frac{S_{\nu 0} D_{\rm L}^2}{(1+z) k_{\rm d}(\nu) B(\nu, T_{\rm dust})} \quad (1)$$

where $k_{\rm d}(\nu) = k_0(\nu/\nu 0)^\beta$ is the dust absorption coefficient. Here we used S_{250}, and $k_{\rm d}$ from Alton et al. (2004). The majority (80%) of the sample is at $\log M_{\rm dust} > 10^8\,M_\odot$ (99% at $> 10^7$) similar to the dust-rich quasars detected in the FIR and (sub)mm (e.g. D12). This value is $\sim$1-2 dex higher than the dust mass estimated for the PG quasars. Therefore, this IR-bright AGN sample is dominated by dusty objects, which are most likely in the process of actively forming stars. **Table 2 lists the derived properties of the IR-bright AGN sample. The full table is available in a machine-readable form in the online journal.**

3.2. *SMBH mass, Eddington Ratios, and BHAR*

Half of the spec-*z* subsample have a spectrum of sufficiently high signal-to-noise to derive reliable virial SMBH masses ($M_\bullet$). The viral SMBH masses are commonly expressed as (e.g. Dai et al. 2014):

$$\log(\frac{M_\bullet}{M_\odot}) = a + b\log(\frac{\lambda L_\lambda}{10^{44}{\rm erg\ s^{-1}}}) + c\log(\frac{\rm FWHM}{\rm km\ s^{-1}}) \quad (2)$$

where $M_\odot$ is the solar mass, FWHM is the full-width-half-maximum of the emission line profile, and λL_λ is the continuum luminosities in 10^{44}erg s^{-1} at 5100 (Hβ, Hα), 3000 (MgII), and 1350 (CIV) Å, respectively. The term λL_λ is used as a proxy for the broad line region radius (Kaspi et al. 2000; Bentz et al. 2013). The coefficients *a* and *b* are empirical values based on SMBH masses determined via the reverberation mapping method, and *c* normally has a fixed value of 2 (e.g. Vestergaard & Peterson 2006). Here we used the FWHM (in km s^{-1}) of the continuum subtracted emission line as the line width proxy, and the factor of 2 for coefficient c exemplifies the virial nature of the broad line region ($M_\bullet \propto Gv^2R^{-1}$). We adopted the IDL line fitting procedures as described in Dai et al. (2014, Sec 3) for CIV (0.660, 0.53, 2.0), MgII (0.740, 0.62, 2.0), Hβ (0.672, 0.61, 2.0), and Hα

[10] http://ydai.caltech.edu/templates/

[11] Note the definition of FIR in Kennicutt (1998) equals the total IR (8–1000 μm). In this work, IR and FIR refer to the range of (8–1000 μm) and (30–1000 μm), respectively.

(0.522, 0.64, 2.06) lines; in brackets are the parameter (a, b, c) sets from Vestergaard & Peterson (2006); Shen et al. (2011); McLure & Dunlop (2004); Greene & Ho (2005), respectively.

From the optical continuum, we also derived the AGN bolometric luminosity L_{AGN}(opt): $L_{AGN}(opt) = k \times \lambda L_{\lambda}$. Here the coefficient k = 9.3, 5.2, and 3.8, for L_{λ} at 5100, 3000, and 1350 Å, respectively (Richards et al. 2006, mean SED for all SDSS quasars). The values of L_{AGN} derived from the X-ray and optical continuum are linearly correlated with a slope of ∼0.45. The offset in the bolometric corrections between X-ray and optical is well known (e.g. Wilkes et al. 1994; Hopkins et al. 2007), and could be affected by obscuration and host galaxy contributions especially for the low *z*, low luminosity sources. This correlation remains the same if only considering the 70% type 1 AGNs of the sample. **To be consistent, in the following discussion the AGN bolometric luminosity and Eddington ratio (ER**= L_{AGN}/L_{edd}**) refer to the values based on the X-ray** L_{AGN}.

For the spec-*z* subsample, we compared the $M_{\bullet}$ **and AGN bolometric luminosity** L_{AGN} **from the X-ray in four fiducial redshift bins (Figure. 2).** Diagonal lines show constant ERs on a log scale. As the redshift increases, the median ER also increases from 0.09 ($0.2 < z < 0.5$), to 0.14 ($0.5 < z < 1.0$), 0.19 ($1.0 < z < 1.5$), and 0.42 ($1.5 < z < 2.5$), respectively. This is an observational bias due to the flux limited nature of the sample. At high *z*, low mass AGNs are generally not detectable unless their ERs are high enough that they lie above the luminosity detection limit. Although such limits are derived from only half of the spec-*z* subsample with reliable $M_{\bullet}$ estimates, it is reasonable to generalize them to the photo-*z* sample where the same flux limits that cause the selection effects also apply. This effect is less prominent at $z < 1.5$, where the ER distribution shows a wide span and scatters into the ER<0.01 region. On the other hand, because of the optical color selections, the SDSS AGNs are biased against low mass, star-forming, disk-dominated galaxies (Trump et al. 2015). Therefore, our SDSS-dominated spec-*z* sample is also affected by this bias. Since $M_{\bullet}$ correlates with the stellar mass of the host galaxy, and therefore the SFR, it is important to bear these selection effects in mind when interpreting the results in Section. 4.

We also calculated the BHAR using the hard L_X as a proxy (e.g. Chen et al. 2013):

$$\frac{\dot{M}_{BH}}{M_{\odot}\,yr^{-1}} = 0.15\frac{\varepsilon}{0.1}\frac{kL_X}{10^{45}erg\,s^{-1}} \quad (3)$$

where ε is the mass-energy conversion efficiency, and *k* is the conversion factor between L_X and the AGN bolometric luminosity. Here we used a k= 22.4 from (Vasudevan & Fabian 2007, based on local AGNs), and a typical ε value of 0.1 (Marconi et al. 2004). These values were chosen to allow direct comparison with other studies (e.g. Chen et al. 2013).

4. RESULTS AND DISCUSSION

4.1. Correlation between AGN activity and Star Formation

In Figure 3, we compare the L_{AGN}-$L_{IR,SF}$ relation of the IR-bright AGNs with references in the literature. Individual objects are plotted as grey dots (X-ray unobscured or optical type 1) or circles (X-ray obscured and optical type 2). The black dash-dotted line shows the best-fit correlation without binning with a slope of 0.60±0.03. A consistent slope within 2σ of 0.65±0.02 is found when the $z < 0.2$ and $z > 2.5$ supplementary sample is included. Our results are in general agreement with the relations using average values in Chen et al. (2013, 2015, brown and light green stars in Fig. 3) and Azadi et al. (2015, dark green stars in Fig. 3) after taking the scatter into account. The Hickox et al. (2014) model (grey shaded area) under-predicts $L_{IR,SF}$ for the luminous IR-bright AGNs in this sample. But since at high *z*, our sample only selects the most luminous objects, inclusion of fainter, yet still 'IR-active' AGNs would lower the average L_{IR} as was the case in Chen et al. (2015) where type 2 AGNs were included (brown stars). Our best-fit correlation overlaps with the correlation based on average values binned by L_{AGN} (blue line, See Sec. 4.2), and with Xu et al. (2015b, X15, dashed orange line). The selection criteria in X15 is comparable to our sample as both require detections in X-ray and FIR, except that X15 has an additional selection based on MIPS $24\mu m$ flux. The $24\mu m$ flux selection is highly complete for AGNs (Krawczyk et al. 2013; Dai et al. 2014), which is again confirmed by the similar fitting results.

We then take advantage of our large sample size and consistent measurements to test for the primary relationship. We run partial Spearman rank analysis (PSRA, e.g. Kendall & Stuart 1976; Akritas & Siebert 1996) between the X-ray and IR properties. PSRA allows for correlation analysis in the general multivariate case, using a matrix of bivariate Spearman rank statistics as input. PSRA tests for correlations between subsamples of the matrix parameters while holding constant all other variables in the matrix. To account for lower limits in our data[12] we use the survival analysis package ASURV (Lavalley et al. 1992) to calculate bivariate Spearman Ranks for input to multivariate PSRA.

We find a strong correlation between $L_{IR,SF}$ and L_{AGN} (probability of a correlation occurring by chance p < 0.01%). The PSRA shows that this is primary due to the strong (p < 0.01%) correlation between the luminosities ($L_{IR,SF}$ or L_{AGN}) and *z*. However, since the correlation between rest-frame X-ray flux and SED-based 60 μm flux density is also strong (p < 0.5%), the observed L_{AGN}- $L_{IR,SF}$ correlation is significant (PSRA p <0.5%) and real. Although simple bivariate correlation analysis also finds a strong correlation between L_{AGN}-$L_{IR,SF}$(p<0.01%), the PSRA shows this to be primary due to the strong correlation between luminosity and *z* (p < 0.5%), with the rest-frame hard X-ray flux and 100 μ m flux density, and the $L_{AGN}$and $L_{IR,SF}$ showing no correlation (p∼9% and p∼26%, respectively). One possible explanation is that the dust emitting at rest-frame 60 μm is warmer, and thus associated with the star formation closer to the nucleus, than the dust emitting at 100 μ m. The lack of such correlation for cooler dust is consistent with the results based on resolved star formation for local Seyfert galaxies (Diamond-Stanic & Rieke 2012). Based on our PSRA (which accounted for the effects of redshift), we conclude that the correlation between L_{AGN} (or L_X) and $L_{IR,SF}$ is significant and real.

We also check the effects of ER and SMBH masses on the L_{AGN}-SFR relation by binning the data by their accretion efficiencies traced by ER and $M_{\bullet}$ (Figure 4). Positive linear correlations are confirmed and do not evolve significantly with ER or $M_{\bullet}$. Since the ERs of AGNs are not evolving significantly between the present day and $z = 4$ (e.g. Dai et al. 2014), the observed relations in the ER are not redshift effects. On the other hand, SMBH mass is well-known to decrease to-

[12] X-ray flux and luminosity were treated as lower limits in sources with HR=1.

wards lower redshift in optical type 1 AGNs (e.g. Labita et al. 2009; Dai et al. 2014). The mass downsizing effect would result in higher L_{AGN} at high z, as demonstrated earlier in Figure. 2. The slopes for different bins are not significantly different (Figure. 4). We conclude that the mass and ER of the SMBH do not regulate the correlation, at least not in a timescale short enough to affect the observed star formation.

As a side note, we emphasize the importance of AGN removal in the IR regime when estimating the SFR. In Figure 3, the 15 detections of X-ray ULIRG/LIRGs from Symeonidis et al. (2011) have systematically higher $L_{\rm IR}$ than in our sample. Besides the fact that these are extremely dusty systems, the IR SED fitting used the Siebenmorgen & Krügel (2007) SED library, as adopted by Symeonidis et al. (2011), was based on starburst systems with limited AGN correction. Similar to Symeonidis et al. (2011), we use the HerMES data, and find an average AGN contribution to the IR luminosity of 47%. Without a careful AGN decomposition, it is unclear whether higher observed $L_{\rm IR}$ is a sign of enhanced star formation. Another caveat is the choice of SFR indicator. Many studies estimated the SFR from single rest-frame FIR photometry, used directly as direct proxy for the star formation component.As discussed in Sec. 3.1, about 20% of the IR-bright AGNs have an AGN-dominated $L_{\rm IR}(8-1000\mu m)$ (10% for $L_{\rm FIR}(30-1000\mu m)$), so that a single data point could still over-estimate the SFR, especially at $\lambda < 30\mu$ m, and in a few special cases at $\lambda > 30\mu$ m. On the other hand, the overall lower Azadi et al. (2015) averaged SFR in Figure. 3 can also be explained by their different approach of SFR estimate. They utilized the *iSEDfit* code (Moustakas et al. 2013), which was based solely on the UV and optical photometry and mainly accounted for unobscured star formation with no AGN removal. As commented in Azadi et al. (2015, Sec 2.3), this method yields systematically lower SFR estimates than using *Hershel* IR data, as the dust extinction and reprocessed dust emission were not accounted for.

4.2. **Binning Effect on the AGN-SFR Correlation**

Given the rapid and significant variability of many AGNs (e.g. Keel et al. 2012), using an instantaneous X-ray luminosity could lead to large scatter that smears out the intrinsic AGN-SF correlation (e.g. Hickox et al. 2014). Several studies have used the average X-ray luminosities and observed a positive correlation between AGN luminosity and SFR (Chen et al. 2013, 2015; Azadi et al. 2015). Different binning criteria would project the intrinsic $L_{\rm AGN}$-SFR relation, if any, onto different axes, and alter the observed slope for any underlying correlations (Volonteri et al. 2015b). **We note that the average values could be biased by the outliers in each bin, especially when stacking is used for non-detections, which is not the case in this work.** In our sample with only detections, the average and median in each luminosity bin are statistically identical, with a K-S test result of $p = 1.0$.

In Fig. 3, we compare the best-fit correlations based on different binning methods. In red is the average $L_{\rm AGN}$ binned by $L_{\rm IR,SF}$, and in blue is the average $L_{\rm IR}$ binned by $L_{\rm AGN}$. Both show a positive correlation with Spearman's coefficients ρ =1.0 ($p < 1e^{-6}$). The average relation binned by $L_{\rm AGN}$ (blue line) agrees well with the correlation without binning (dot-dashed black line). Compared to the $L_{\rm X}$ bins (slope $k = 0.58 \pm 0.13$), a tighter correlation with a steeper slope is observed using $L_{\rm IR,SF}$ bins ($k = 1.57 \pm 0.09$). This is consistent with the variability argument that the star formation varies more slowly than the AGN, e.g. it can vary by a factor of 100 on timescales of 100 Myr (Hickox et al. 2014). This scenario could explain the lack of such correlation when the sample were AGN selected (e.g. Volonteri et al. 2015b). Table 3 summarizes the average properties in each luminosity bin.

4.3. **Redshift Effect on the AGN-SFR Correlation**

Besides the PSRA results discussed earlier, in this section we further investigate the redshift effect. As confirmed by several studies, the SFR in AGN hosts increases strongly with redshift (e.g. Mullaney et al. 2012a), and it has been argued that the observed positive correlation between $L_{\rm IR,SF}$ and $L_{\rm AGN}$ is a combination of redshift effect and Malmquist bias. Figure 5 shows the least square linear fit between $L_{\rm AGN}$ and $L_{\rm IR,SF}$ in four fiducial redshift bins: $0.2 < z < 0.5$, $0.5 < z < 1.0$, $1.0 < z < 1.5$, and $1.5 < z < 2.5$. Crosses mark the hard AGNs with HR=1 (detected only in the hard band), whose $L_{\rm X}$ are lower limits. These hard IR-bright AGNs occupy the same space as the rest of the sample, showing no systematical difference. A test correction of these objects by a factor of 2 results in an increase of the normalization factor, but both normalization and slope of the correlation are consistent within errors. The solid and dashed lines mark the linear fit in each redshift bin. The IR-bright AGNs distribution is in general agreement with the Netzer (2009) relation (dashed line) extrapolated from local type 2 AGNs, but show higher $L_{\rm IR,SF}$ at low z. Without binning, the correlations between $L_{\rm X}$ and $L_{\rm IR,SF}$ are weak but positive. The Spearman's tests yield a rank correlation coefficient ρ =0.73 with significance p=0 (ρ =1 or $p = 0$ indicates a perfectly monotonic relation), indicating a strong correlation from $0.2 < z < 2.5$ (dash-dotted line, same as in Figure 3). In discrete redshift bins, the correlations are weaker with p = 0.005%, 0.07%, 20.7%, and 1% (z from low to high). If only considering the unobscured AGNs, the correlations become weaker, but still significant, with p = 0.5%, 1.6%, 20.7%, and 0.4%. At $z > 1.0$ the correlation is not significant, possibly due to the selection effect discussed in Sec. 2.1. At high z, the range in luminosity is smaller as less luminous, low ER AGNs fall below the flux detection limits, making it harder to observe a significant correlation due to the smaller parameter range, possibly due to the Malmquist bias discussed in Sec. 2.1. The correlations in smaller redshift bins are flatter and weaker than the overall correlation (Figure. 3)s, consistent with the removal of the redshift effect as shown by the PSRA results.

To investigate the effect of the flux limits in a given redshift range, we calculate the average $L_{\rm IR,SF}$ in bins of $L_{\rm AGN}$ for each redshift bracket (Figure. 6, left). Despite the overall increasing trend, the slopes are not well constrained. We do not observe an enhanced SF at low AGN luminosity, as reported in previous studies (e.g. Shao et al. 2010; Rosario et al. 2012; Matsuoka & Woo 2015). The observed enhancement of star formation at high $L_{\rm AGN}$ in Figure. 6 is likely affected by the Malmquist bias as discussed above. An IR-bright AGN with lower ER would be IR-undetected at high z, and the inclusion of these objects would flatten the observed correlation. In this study we choose not to stack the IR non-detections to avoid contamination from 'IR-quiescent' AGNs (See Sec. 3.1). Since we do not know the intrinsic distribution of IR-bright and IR-quiescent AGNs, using IR stacking could smear out any intrinsic correlation between AGN

and star formation with the inclusion of IR-quiescent AGNs. This could possibly explain the flat or no correlation found in Stanley et al. (2015), where 75% of the data points are IR upper limits. In fact, according to simulations, e.g. in merger-driven models (Hopkins et al. 2006), AGNs are only 'FIR-luminous', aka, IR-bright, for a short period of their lifetime. Therefore, correlations based on stacked FIR data are likely biased towards IR-quiescent, normal AGNs, which have limited or no ongoing star forming, and thus result in a flat or non-correlation.

In Figure. 6 (right) we plot the $L_{\rm AGN}$ in bins of $L_{\rm IR,SF}$ for the IR-bright AGNs in different redshift ranges. We confirm that using the $L_{\rm IR,SF}$ bins results in tighter and steeper correlations, as discussed in Section. 4.2.

4.4. *A constant ratio between SFR and BHAR*

To test if the correlation evolves with redshift or $M_\bullet$, we compare the relative strength of star formation and AGN, represented by the ratio of the AGN-removed $L_{\rm IR,SF}$ and $L_{\rm X}$. Despite the large scatter, we find a constant ratio between the luminosities (Figure 7, top):

$$\log(L_{\rm IR,SF}/L_{\rm X}) = (1.82\pm0.05)+(0.03\pm0.04)z \quad (4)$$

$$\log(L_{\rm IR,SF}/L_{\rm X}) = (1.97\pm0.52)+(-0.01\pm0.06)M_\bullet \quad (5)$$

with a standard deviation of 0.57 and 0.55, respectively. The luminosity ratio remains constant from z =0 to z =2.5, and does not change with redshift or $M_\bullet$. As noted earlier, at higher redshift our sample is incomplete to fainter, IR-bright AGN and thus the intrinsic relation could be flatter. We also find that at the same $L_{\rm IR,SF}/L_{\rm X}$ ratio, the AGN contribution to the total IR luminosity (f= $L_{\rm IR,AGN}/L_{\rm IR}$, see Sec. 3.1 for details) ranges from insignificant (<0.2) to dominant (>0.5), confirming the importance of AGN decomposition in the IR regime. Inclusion of the $z<0.2$ and $z>2.5$ supplement sample yields consistent results.

The constant luminosity ratios indicate constant energy output ratios between the SMBH and star formation component, consistent with the scenario of a common source of gas supply that feeds the SMBH and host simultaneously. This is confirmed by the SFR/BHAR ratios (Figure 7, middle). Up to $z=2.5$, the IR-bright AGN sample shows a non-zero ratio of:

$$\log({\rm SFR}/{\rm BHAR}) = (2.82\pm0.04)+(0.07\pm0.03)z \quad (6)$$

$$\log({\rm SFR}/{\rm BHAR}) = (2.88\pm0.41)+(0.01\pm0.05)M_\bullet \quad (7)$$

with a standard deviation of 0.57 and 0.55, respectively. Since the SFR/BHAR vs $M_\bullet$ relation is based on the subsample of type 1 AGNs with a secure $M_\bullet$ estimate, we also fitted the SFR/BHAR vs z for the full type 1 subsample and found a comparable constant ratio of (2.88±0.05), with a standard deviation of 0.55. This $\dot{M}$ ratio (SFR/BHAR) remains flat over redshift and BH mass, and coincides with the mass ratios found in local galaxies. The ratio in Eq. 7 is biased by the requirement of a reliable $M_\bullet$ estimate, where only luminous, high ER AGNs are included. The BH-host mass relation is well-established at low z to be around $\log(M_{\rm bulge}/M_\bullet)$=2.81±0.36 (Marconi & Hunt 2003), sometimes with higher but consistent values at $\log(M_{\rm bulge}/M_\bullet)$=2.90±0.45 (Merritt & Ferrarese 2001; McLure & Dunlop 2002). Since the $\log(M_{\rm bulge}/M_{*,\rm total})$ ratio is around -0.15 (Mendel et al. 2014, median for 660,000 SDSS DR7 galaxies). we adopt this value to convert the BH-bulge relation to $\log(M_*/M_\bullet)$=(2.96±0.36) and $\log(M_*/M_\bullet)$=(3.05±0.45) (blue and green dashed lines in Figure 7), both consistent with the ratio found for the IR-bright AGNs. It is worth noting that significantly different mass ratios have also been reported before, e.g. $\log(M_*/M_\bullet)$=2.6±0.4 (Kormendy & Ho 2013), and $\log(M_*/M_\bullet)$=3.6±0.5 (Reines & Volonteri 2015). The mass differences arise from the different parent sample used to derive the relation, e.g., Reines & Volonteri (2015) were dominated by local spiral galaxies instead of ellipticals used in earlier studies. The different methods used to derive $M_\bullet$ also contributed to the different results, and cannot be compared directly to our sample. Not all IR-bright galaxies are AGNs, e.g. only 10-30% of the (ultra-) luminous IR galaxies—(U)LIRGs—are AGNs according to simulations and observations (e.g. Fu et al. 2010; Hopkins 2012), and vice versa, not all AGNs are IR-bright (See also Sec. 2). As a consequence, the AGN's relative life time between the IR-bright and IR-quiescent phases would result in different accumulated mass ratios, as the host galaxy stellar mass could be similar between the IR-detected and IR-undetected populations (e.g. Santini et al. 2012; Rovilos et al. 2012; Rosario et al. 2013a). Inclusion of the $z<0.2$ and $z>2.5$ supplement sample yields consistent results, indicating limited redshift bias to this constant mass forming ratio.

Compared to the literature values for the $\log(M_*/M_\bullet)$ ratios (blue and green lines in Figure 7), the IR-bright AGN sample shows a larger scatter. This could be due to one or more of the following factors: a. uncertainties in the SFR and BHAR estimates; b. the large variability of the instantaneous ratios; c. the unknown host galaxy morphology—the sample is not restricted to bulges and ellipticals, and could include spirals and other types, which may not share the same mass ratios (Kormendy & Ho 2013). Actually, **the $\log(M_{\rm bulge}/M_{*,\rm total})$ ratio quoted above could possibly underestimate the total stellar mass, as systematically higher masses have been reported for AGN hosts than typical SDSS galaxies (e.g. Kauffmann et al. 2003). But the mean log (SFR/BHAR) ratio is not affected by the mass estimates and remains constant regardless of redshift or stellar mass**, indicating a relatively stable nucleus-host connection and favoring the secular evolution picture where BH and galaxies form via steady gas accretion. Since the duty cycles could differ significantly between the AGN phase and the star formation phase, the coincidence found in our results indicates that on average, BH and host galaxy are moving along the same mass ratio planes, regardless of the level of activity of the galaxy. This suggests that the same physical processes and the bulge-BH mass relations hold on an average basis, at least up to $z=2.5$ for IR-bright AGNs. In other words, as long as the host galaxy is actively forming stars, ∼1% of the mass funnels into the nuclear region and feeds the BH accretion. For young systems after the IR-bright AGN phase, where star formation has slowed down or been quenched by possible feedback, the AGN would continue accreting masses and decrease the $M_*/M_\bullet$ for a short period of time, before the BH accretion slows down and star formation dominates again. Vice versa, before the IR-bright AGN phase, due to the generally shorter X-ray duty cycle, the system would have already accumulated stellar mass and obtained a high $M_*/M_\bullet$ value. Adjusting the duty cycles on and off the IR-bright AGN phase could explain the ∼1 dex range in mass ratios reported in different published studies. Our results are in general agreement with Mullaney et al. (2012b), but with a statistically more significant sample (10× larger) and a wider redshift coverage. Such results have also been

predicted by simulations, where the galaxy and BH can be modulated by torque-limited growth along the bulge-BH mass plane from $z=4$ to $z=0$ (Anglés-Alcázar et al. 2015).

5. SUMMARY

We constructed a sample of 828 IR-bright AGNs with $L_X > 10^{42}$erg s^{-1} at $0.2 < z < 2.5$ in the ~ 10 deg^2 XMM-LSS field. All targets are detected in both hard X-ray and FIR and have either spec-z (58%) or photo-z (42%). The majority of the sources (66%) are unobscured type 1 objects, and 80% of the sample have dust mass greater than $10^8\,M_\odot$, making it a dusty, type 1 dominant AGN sample. For these IR-bright AGNs, we find a weak AGN-SFR correlation after removing the redshift effects. This correlation is more significant using the average values binned by IR luminosities than AGN luminosities. This is consistent with the scenario that the AGN luminosity varies on a shorter timescale than the SF in the galaxy. We do not find significant diversity in the observed correlation for subsets based on black hole mass or ERs. Constant ratio is observed between the SFR and BHAR, regardless of redshift or SMBH mass. These findings support the coevolution picture where IR-bright AGNs are growing in step with the host galaxy from the same fueling source at a constant rate, possibly due to the same physical mechanism. The shutting down of the star formation by AGN 'feedback', if any, takes considerably more time than the gas depletion time. The mean and standard deviation of the log(SFR/BHAR) ratio in IR-bright AGNs is $\sim$2.82, with a scatter of 0.57, consistent with the log($M_*/M_\bullet$) ratios found for local galaxies. Inclusion of $z < 0.2$ and $z > 2.5$ IR-bright AGNs yields consistent ratios, indicating limited redshift effect on this mass accretion ratio. Despite the large scatter in the distribution of instantaneous log(SFR/BHAR) ratios, this constant mean ratio observed in IR-bright AGNs indicates a universal bulge-BH mass relation up to $z=2.5$. Our results support a secular evolution picture where both the black hole and host galaxy are fed by a common gas supply at a relatively constant rate when the gas is available.

Y.S.D would like to thank Lee Armus, Nick Scoville, Phillip Hopkins, Chris Hayward, Marta Volonteri, and Ranga R. Chary for helpful discussions. This research has made use of data from HerMES project (http://hermes.sussex.ac.uk/). HerMES is a Herschel Key Programme utilising Guaranteed Time from the SPIRE instrument team, ESAC scientists and a mission scientist. The HerMES data was accessed through the Herschel Database in Marseille (HeDaM - http://hedam.lam.fr) operated by CeSAM and hosted by the Laboratoire d'Astrophysique de Marseille.

REFERENCES

Alton, P. B., Xilouris, E. M., Misiriotis, A., Dasyra, K. M., & Dumke, M. 2004, å, 425, 109
Alexander, D. M., & Hickox, R. C. 2012, New A Rev., 56, 93
Akritas, M. G. & Siebert, J., 1996, MNRAS, 278, 919
Anglés-Alcázar, D., Özel, F., Davé, R., et al. 2015, ApJ, 800, 127
Azadi, M., Aird, J., Coil, A. L., et al. 2015, ApJ, 806, 187
Barger, A. J., Cowie, L. L., Owen, F. N., et al. 2015, ApJ, 801, 87
Beelen, A., Cox, P., Benford, D. J., et al. 2006, ApJ, 642, 694
Bentz, M. C., Denney, K. D., Grier, C. J., et al. 2013, ApJ, 767, 149
Blain, A. W., Barnard, V. E., & Chapman, S. C. 2003, MNRAS, 338, 733
Bournaud, F., Dekel, A., Teyssier, R., et al. 2011, ApJ, 741, L33
Bower, R. G., Benson, A. J., Malbon, R., et al. 2006, MNRAS, 370, 645
Chen, C.-T. J., Hickox, R. C., Alberts, S., et al. 2013, ApJ, 773, 3
Chen, C.-T. J., Hickox, R. C., Alberts, S., et al. 2015, ApJ, 802, 50
Chiappetti, L., Clerc, N., Pacaud, F., et al. 2013, MNRAS, 429, 1652, C13
Croom, S. M., Richards, G. T., Shanks, T., et al. 2009, MNRAS, 399, 1755
Dai, Y. S., Bergeron, J., Elvis, M., et al. 2012, ApJ, 753, 33, D12
Dai, Y. S., Elvis, M., Bergeron, J., et al. 2014, ApJ, 791, 113, D14
Debuhr, J., Quataert, E., & Ma, C.-P. 2012, MNRAS, 420, 2221
Diamond-Stanic, A. M., & Rieke, G. H. 2012, ApJ, 746, 168
Di Matteo, T., Springel, V., & Hernquist, L. 2005, Nature, 433, 604
Elbaz, D., Daddi, E., Le Borgne, D., et al. 2007, A&A, 468, 33
Elbaz, D., Dickinson, M., Hwang, H. S., et al. 2011, A&A, 533, A119
Ferrarese, L., & Merritt, D. 2000, ApJ, 539, L9
Fiore, F., Puccetti, S., Brusa, M., et al. 2009, ApJ, 693, 447
Fu, H., Yan, L., Scoville, N. Z., et al. 2010, ApJ, 722, 653
Gandhi, P., Horst, H., Smette, A., et al. 2009, A&A, 502, 457
Greene, J. E., & Ho, L. C. 2005, ApJ, 630, 122
N. Z., et al. 2010, ApJ, 722, 653
Harrison, C. M., Alexander, D. M., Mullaney, J. R., et al. 2012, ApJ, 760, L15
Hickox, R. C., Mullaney, J. R., Alexander, D. M., et al. 2014, ApJ, 782, 9
Hopkins, P. F., Hernquist, L., Cox, T. J., et al. 2006, ApJS, 163, 1
Hopkins, P. F., Richards, G. T., & Hernquist, L. 2007, ApJ, 654, 731
Hopkins, P. F. 2012, MNRAS, 420, L8
Kaspi, S., Smith, P. S., Netzer, H., et al. 2000, ApJ, 533, 631
Kauffmann, G., Heckman, T. M., Tremonti, C., et al. 2003, MNRAS, 346, 1055
Keel, W. C., Chojnowski, S. D., Bennert, V. N., et al. 2012, MNRAS, 420, 878
Kendall, M., & Stuart, A. 1976, London: Griffin, 1976, 3rd ed.
Kennicutt, R. C., Jr. 1998, ARA&A, 36, 189
Kormendy, J., & Richstone, D. 1995, ARA&A, 33, 581
Kormendy, J., & Ho, L. C. 2013, ARA&A, 51, 511
Krawczyk, C. M., Richards, G. T., Mehta, S. S., et al. 2013, ApJS, 206, 4
Labita, M., Decarli, R., Treves, A., & Falomo, R. 2009, MNRAS, 396, 1537
Lanzuisi, G., Piconcelli, E., Fiore, F., et al. 2009, A&A, 498, 67
Lavalley, M. P., Isobe, T., & Feigelson, E. D. 1992, BAAS, 24, 839
Lonsdale, C. J., Smith, H. E., Rowan-Robinson, M., et al. 2003, PASP, 115, 897
Lutz, D., Maiolino, R., Spoon, H. W. W., & Moorwood, A. F. M. 2004, A&A, 418, 465
Lutz, D., Mainieri, V., Rafferty, D., et al. 2010, ApJ, 712, 1287
Madau, P., & Dickinson, M. 2014, ARA&A, 52, 415
Magorrian, J., Tremaine, S., Richstone, D., et al. 1998, AJ, 115, 2285
Marconi A., Hunt L. K., 2003, ApJ, 589, L21
Marconi, A., Risaliti, G., Gilli, R., et al. 2004, MNRAS, 351, 169
Mateos, S., Carrera, F. J., Alonso-Herrero, A., et al. 2015, MNRAS, 449, 1422
Matsuoka, K., & Woo, J.-H. 2015, ApJ, 807, 28
McLure, R. J., & Dunlop, J. S. 2002, MNRAS, 331, 795
Melnyk, O., Plionis, M., Elyiv, A., et al. 2013, A&A, 557, A81, M13
Mendel, J. T., Simard, L., Palmer, M., Ellison, S. L., & Patton, D. R. 2014, ApJS, 210, 3
Merloni A., Rudnick G., Di Matteo T. 2004, MNRAS, 354, L37
Merritt, D., & Ferrarese, L. 2001, MNRAS, 320, L30
Moustakas, J., Coil, A. L., Aird, J., et al. 2013, ApJ, 767, 50
McLure, R. J., & Dunlop, J. S. 2004, MNRAS, 352, 1390 & Hickox, R. C. 2011, MNRAS, 414, 1082
Mullaney, J. R., Pannella, M., Daddi, E., et al. 2012a, MNRAS, 419, 95
Mullaney, J. R., Daddi, E., Béthermin, M., et al. 2012b, ApJ, 753, L30
Nandra, K., & Pounds, K. A. 1994, MNRAS, 268, 405
Netzer, H. 2009, MNRAS, 399, 1907
Noeske, K. G., Weiner, B. J., Faber, S. M., et al. 2007, ApJ, 660, L43
Oliver et al. 2012, MNRAS, 424,1614
Page, M. J., Symeonidis, M., Vieira, J. D., et al. 2012, Nature, 485, 213
Pannella, M., Carilli, C. L., Daddi, E., et al. 2009, ApJ, 698, L116
Pierre, M., Chiappetti, L., Pacaud, F., et al. 2007, MNRAS, 382, 279
Podigachoski, P., Barthel, P. D., Haas, M., et al. 2015, A&A, 575, A80
Priddey, R. S., Isaak, K. G., McMahon, R. G., & Omont, A. 2003, MNRAS, 339, 1183
Ranalli, P., Comastri, A., & Setti, G. 2003, A&A, 399, 39
Ranalli, P., Koulouridis, E., Georgantopoulos, I., et al. 2015, arXiv:1512.05563
Reines, A. E., & Volonteri, M. 2015, ApJ, 813, 82
Richards, G. T., et al. 2006, ApJS, 166, 470

TABLE 1
THE RANGE OF X-RAY AND IR LUMINOSITIES IN BINS OF REDSHIFT

Redshift bins	$0.2 < z \leq 0.5$	$0.5 < z \leq 1.0$	$1.0 < z \leq 1.5$	$1.5 < z \leq 2.5$	Total
All Hard Xray & Herschel detected*	137 (49%)	249 (39%)	227 (35%)	215 (36%)	828 (38%)
spec-z subsample	102	151	109	121	483
photo-z subsample	35	98	118	94	345
X-ray Luminosity ($\log L_X$, erg s^{-1})					
42.0-43.0	60	4	...	...	64
43.0-44.0	72	179	43	3	297
44.0-45.0	5	66	181	178	430
> 45.0	...	...	3	34	37
IR luminosity ($\log L_{IR,SF}$, $L_\odot$)					
$< 11.0^\dagger$	66	8	1	2	77
11.0 - 12.0	57	155	41	5	258
12.0 - 13.0	7	74	156	121	357
> 13.0	...	...	11	54	65

Notes: *: in 2XLSSd overlapping region only. In parenthesis are the percentage in the 2,399 hard X-ray detected AGNs in the same redshift range. †: excluding the 70 objects whose L_{IR} is purely from AGN heating.

TABLE 2
DERIVED PROPERTIES FOR IR-BRIGHT AGNS*

Xcatname	redshift	zflag	Td (K)	α	HR	N_H (int) (cm^{-2})	L_X (erg s^{-1})	flag	$L_{IR,SF}$ (erg s^{-1})	SFR ($M_\odot$ yr^{-1})	logMd ($M_\odot$)
(1)	(2)	(3)	(4)	(5)	(6)	(7)	(8)	(9)	(10)	(11)	(12)
2XLSSd J021809.6-050159	1.275	1	27.2±1.6	2.0±0.1	0.14	5.818e+22	43.60	1	46.36±1.00	1020	9.2±1.4

Notes: (1) Object identification same as in Chiappetti et al. (2013). (2) Redshift of the object. (3) Redshift flag, 1 for spec-z, 2 for photo-z. (4) & (5) Peak dust temperature and power-law index derived from SED fitting as described in Sec. 3.1. (6) Hardness ratio (HR=(H − S)/(H + S)) based on count rates. (7) Intrinsic column density derived from redshift and HR as described in Sec. 2. If the object is only detected in the hard X-ray, a value of 1.00e+23+ is assigned. If the object has an HR < -0.5, no N_H correction was made and a value of '0' was assigned. (8) Obscuration corrected rest-frame X-ray luminosity (2-10 keV). (9) Hard X-ray detection flag as defined in C13, 0 if MOS−pn difference is <20%, 1 between 20% and 50%, 2 above 50%. (10) AGN-subtracted infrared luminosity (8-1000 μm). A value of '0' marks purely AGN driven IR luminosity. (11) SFR derived from (10) using the Kennicutt (1998) relation. A value of '0' marks purely AGN driven IR luminosity. (12) Dust mass derived from FIR photometry as described in Sec. 3.1. *: Low ($z < 0.2$) and high ($z > 2.5$) IR-bright sources are also included. This table is available in its entirety with a machine-readable form in the online journal.

TABLE 3
DERIVED AVERAGE PROPERTIES IN EACH LUMINOSITY BIN

luminosity range (1)	N_{det} (2)	z range (3)	$< logL_{AGN} >$ (4)	$< logL_{IR,SF} >$ (5)	$< logM_{BH} >$ (6)	$< ER >$ (7)
binned by L_{AGN}						
43.0-43.5	13	0.200-0.468	$43.34^{+0.33}_{-0.43}$	$44.50^{+1.06}_{-0.75}$	$6.22^{+0.13}_{-0.15}$	$0.09^{+0.01}_{-0.01}$
43.5-44.0	40	0.200-0.670	$43.79^{+0.41}_{-0.42}$	$44.42^{+1.57}_{-1.08}$	$7.66^{+2.08}_{-1.47}$	$0.15^{+0.38}_{-0.15}$
44.0-44.5	75	0.205-0.900	$44.28^{+0.42}_{-0.48}$	$44.97^{+1.52}_{-1.87}$	$7.50^{+1.67}_{-1.43}$	$0.25^{+0.56}_{-0.24}$
44.5-45.0	120	0.238-1.399	$44.77^{+0.42}_{-0.46}$	$45.21^{+1.52}_{-1.68}$	$8.00^{+1.35}_{-1.11}$	$0.10^{+0.33}_{-0.09}$
45.0-45.5	127	0.292-2.023	$45.26^{+0.44}_{-0.45}$	$45.51^{+1.11}_{-1.49}$	$8.17^{+1.22}_{-0.77}$	$0.17^{+0.61}_{-0.16}$
45.5-46.0	162	0.480-2.330	$45.76^{+0.44}_{-0.45}$	$45.93^{+1.19}_{-1.68}$	$8.49^{+0.68}_{-0.64}$	$0.20^{+0.38}_{-0.17}$
46.0-46.5	152	0.779-2.480	$46.23^{+0.47}_{-0.43}$	$46.09^{+1.09}_{-2.05}$	$8.74^{+0.94}_{-0.66}$	$0.34^{+0.51}_{-0.29}$
46.5-47.0	52	0.874-2.456	$46.75^{+0.44}_{-0.43}$	$46.31^{+1.00}_{-1.85}$	$9.21^{+0.39}_{-0.35}$	$0.31^{+0.52}_{-0.16}$
47.0-47.5	14	1.655-2.327	$47.18^{+0.42}_{-0.35}$	$46.56^{+0.36}_{-0.57}$	$9.26^{+0.12}_{-0.15}$	$0.59^{+0.10}_{-0.15}$
binned by $L_{IR,SF}$						
43.0-43.5	5	0.214-0.290	$44.12^{+0.29}_{-0.46}$	$43.32^{+0.15}_{-0.22}$	$6.85^{+0.79}_{-0.79}$	$0.41^{+0.39}_{-0.39}$
43.5-43.0	10	0.200-0.515	$43.94^{+1.04}_{-0.82}$	$43.86^{+0.13}_{-0.33}$	$6.07^{+0.00}_{-0.00}$	$0.09^{+0.00}_{-0.00}$
44.0-44.5	52	0.200-1.663	$44.31^{+2.33}_{-1.01}$	$44.30^{+0.19}_{-0.29}$	$7.93^{+1.46}_{-1.69}$	$0.08^{+0.17}_{-0.08}$
44.5-44.0	107	0.200-1.275	$44.65^{+1.58}_{-1.68}$	$44.78^{+0.22}_{-0.28}$	$7.73^{+1.01}_{-1.66}$	$0.19^{+0.57}_{-0.18}$
45.0-45.5	134	0.225-2.327	$45.13^{+1.81}_{-1.80}$	$45.27^{+0.23}_{-0.26}$	$7.91^{+0.73}_{-1.72}$	$0.25^{+0.60}_{-0.23}$
45.5-45.0	186	0.343-2.198	$45.57^{+1.65}_{-2.14}$	$45.76^{+0.24}_{-0.26}$	$8.39^{+1.36}_{-1.05}$	$0.21^{+0.56}_{-0.21}$
46.0-46.5	180	0.289-2.381	$45.91^{+1.49}_{-1.67}$	$46.23^{+0.27}_{-0.23}$	$8.67^{+0.70}_{-1.19}$	$0.22^{+0.53}_{-0.22}$
46.5-46.0	73	1.078-2.480	$46.35^{+1.02}_{-1.43}$	$46.72^{+0.28}_{-0.21}$	$8.90^{+0.70}_{-0.59}$	$0.33^{+0.51}_{-0.30}$
47.0-47.5	9	1.507-2.452	$46.52^{+0.45}_{-0.79}$	$47.13^{+0.18}_{-0.12}$	$9.23^{+0.45}_{-0.67}$	$0.27^{+0.25}_{-0.23}$

Notes: *: only one object with $M_\bullet$ estimate in this luminosity bin. (1)Luminosity range in erg s^{-1}, (2) number of X-ray and FIR detected IR-bright AGNs, (3) redshift range for objects in the subgroup, (4) average AGN bolometric luminosity in erg s^{-1}, (5) average IR luminosity from star formation in erg s^{-1}, (6) average SMBH mass in $M_\odot$ for subsample in the bin with a mass estimate, (7) average Eddington ratio for subsample in the bin with a mass estimate. The errors in column (4)-(7) indicate the *range* for the binned objects.

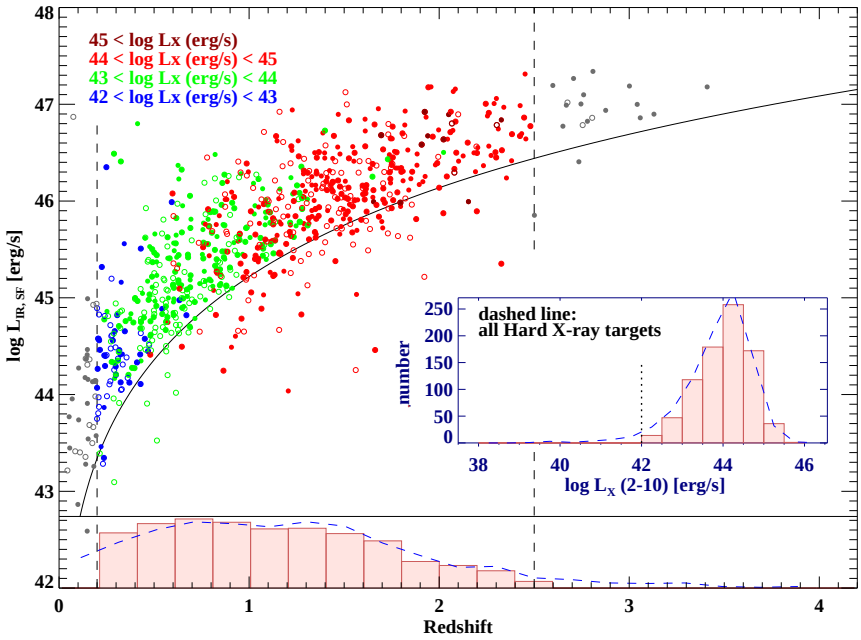

FIG. 1.— The AGN corrected infrared luminosity ($L_{\rm IR,SF}$) and redshift distribution of the sample of 828 IR-bright AGNs at $0.2 < z < 2.5$, color coded by the $L_{\rm X}$, as labelled in the legend. In grey we plot the supplement sample of IR-bright AGNs at $z < 0.2$ and $2.5 < z < 4.2$ as a reference. Filled circles mark the unobscured AGNs (X-ray unobscured or optical type 1), which contributes to 66% of the full sample. Open circles are the obscured AGNs (X-ray obscured or optical type 2). The black curve shows the 3σ detection limit in the FIR, some data fall below the limit because of the AGN correction as described in Sec. 3.1. The right inset shows the absorption corrected hard X-ray luminosity $L_{\rm X}$ (2-10 keV) distribution of the sample. The dotted line marks the luminosity cut at $L_{\rm X} = 10^{42}$ erg s^{-1}. The $L_{\rm X}$ of this sample spans 4 orders of magnitude from $10^{42.0} - 10^{45.6}$ erg s^{-1}, peaking at a median of $10^{44.1}$ erg s^{-1}. The bottom inset shows the redshift distribution of the sample, with the dashed line for all 2,399 hard X-ray detections (scaled). Majority (93%) of the sample lies within the redshift range of $0.2 < z < 2.5$. The higher frequency of $0.2 < z < 0.8$ objects in our sample is because the spec-z subsample covers a high fraction of low-z objects; and the decrease in the number of objects at $z < 0.2$ is due to the $L_{\rm X}$ cut at $10^{42.0}$ erg s^{-1}. IR-bright AGNs share a similar z and $L_{\rm X}$ distribution as the parent sample of hard X-ray detected targets (blue dashed line).

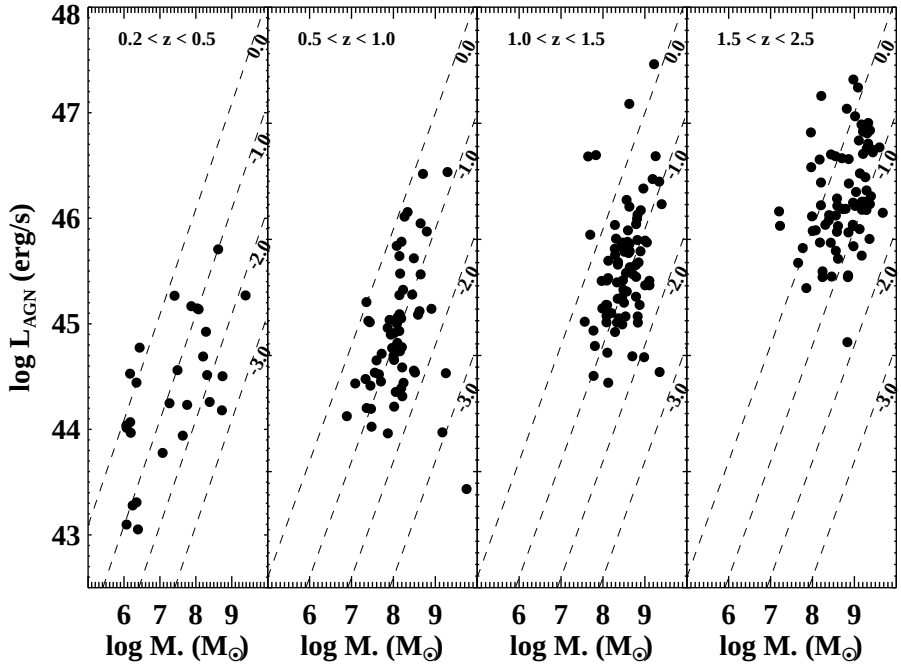

FIG. 2.— The AGN bolometric luminosity vs. SMBH mass ($M_\bullet$) in 4 fiducial redshift bins for the subsample of IR-bright AGNs with reliable BH mass estimates (∼50% of the spec-z subsample). Dashed lines mark the Eddington ratios (ERs) at 1, 0.1, 0.01, and 0.001, and are labeled by log (ER). At $z < 1.0$, the IR-bright AGN sample has a wide span of ER to ER < 0.01, but at high z, the sample is limited to massive, high ER AGNs. The median ER increases with z, from 0.09 ($0.2 < z < 0.5$), to 0.14 ($0.5 < z < 1.0$), 0.19 ($1.0 < z < 1.5$), and 0.42 ($1.5 < z < 2.5$), respectively.

Rodighiero, G., Daddi, E., Baronchelli, I., et al. 2011, ApJ, 739, L40
Rosario, D. J., Santini, P., Lutz, D., et al. 2012, A&A, 545, A45
Rosario, D. J., Santini, P., Lutz, D., et al. 2013a, ApJ, 771, 63
Rosario, D. J., Trakhtenbrot, B., Lutz, D., et al. 2013b, A&A, 560, A72
Roseboom et al. 2010, MNRAS, 409, 48
Roseboom et al. 2012, MNRAS, 419,2758
Rovilos, E., Comastri, A., Gilli, R., et al. 2012, A&A, 546, A58
Santini, P., Rosario, D. J., Shao, L., et al. 2012, A&A, 540, A109
Shao, L., Lutz, D., Nordon, R., et al. 2010, A&A, 518, L26
Shen, Y., Richards, G. T., Strauss, M. A., et al. 2011, ApJS, 194, 45 (S11)
Shimizu, T. T., Mushotzky, R. F., Meléndez, M., Koss, M., & Rosario, D. J. 2015, MNRAS, 452, 1841
Siebenmorgen, R., & Krügel, E. 2007, A&A, 461, 445
Silk, J., & Rees, M. J. 1998, A&A, 331, L1
Silverman, J. D., Green, P. J., Barkhouse, W. A., et al. 2008, ApJ, 679, 118
Springel, V., White, S. D. M., Jenkins, A., et al. 2005, Nature, 435, 629
Stanley, F., Harrison, C. M., Alexander, D. M., et al. 2015, MNRAS, 453, 591
Stern, D. 2015, ApJ, 807, 129
Symeonidis, M., Georgakakis, A., Seymour, N., et al. 2011, MNRAS, 417, 2239
Szokoly, G. P., Bergeron, J., Hasinger, G., et al. 2004, ApJS, 155, 271
Trump, J. R., Sun, M., Zeimann, G. R., et al. 2015, ApJ, 811, 26
Vasudevan, R. V., & Fabian, A. C. 2007, MNRAS, 381, 1235
Vestergaard, M., & Peterson, B. M. 2006, ApJ, 641, 689 (VP06)
Volonteri, M., Capelo, P. R., Netzer, H., et al. 2015a, MNRAS, 449, 1470
Volonteri, M., Capelo, P. R., Netzer, H., et al. 2015b, MNRAS, 452, L6
Wang, L., Viero, M., Clarke, C., et al. 2014, MNRAS, 444, 2870
Wilkes, B. J., Tananbaum, H., Worrall, D. M., et al. 1994, ApJS, 92, 53
Xu, L., Rieke, G. H., Egami, E., et al. 2015a, ApJ, 808, 159
Xu, L., Rieke, G. H., Egami, E., et al. 2015b, ApJS, 219, 18, X15

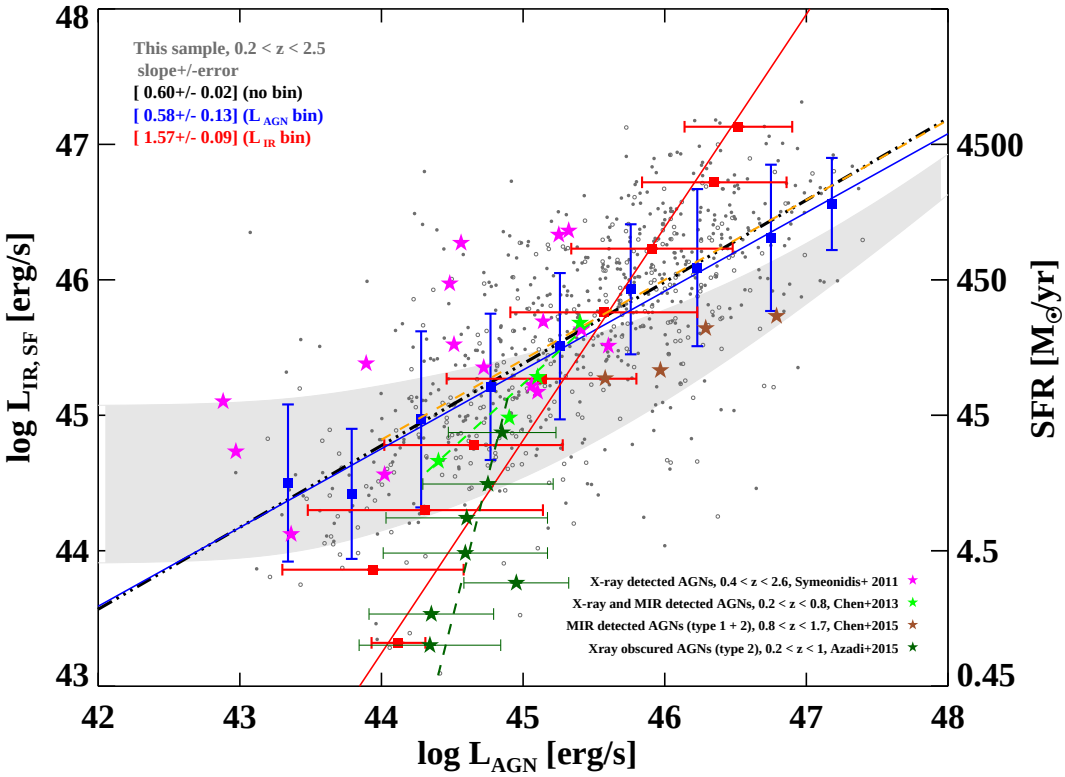

FIG. 3.— Correlation between theL_{AGN} and $L_{IR,SF}$ for the IR-bright AGNs. In blue is the average L_{AGN} plotted in bins of SFR ($L_{IR,SF}$), in red is the average L_{IR} plotted in bins of AGN (L_{AGN}), and in dash-dotted black line is the best fit correlation without binning. Individual IR-bright AGNs are plotted as grey dots as in Figure. 1. Binning the data by SFR results in a steeper positive correlation, consistent with the shorter AGN variability argument proposed in Volonteri et al. (2015a,b). The shaded region marks the Hickox et al. (2014) relation at $0.01 < z < 3.5$. Also plotted are the literature data of IR-bright AGNs: pink stars are the X-ray and FIR detected AGNs from Symeonidis et al. (2011), green and brown stars are the X-ray and MIR detected AGNs from Chen et al. (2013, 2015), the dark green green stars are the X-ray obscured AGNs from Azadi et al. (2015). Dashed light green, dark green, and orange lines mark the literature correlations in Chen et al. (2013), Azadi et al. (2015), and Xu et al. (2015b), respectively. Our results are in general agreement with Chen et al. (2013). The correlations without binning, binned by L_{AGN}, and from Xu et al. (2015b) overlap with each other. We discussed the relative selection effects and caveats that could cause the different slopes in Sec. 4.

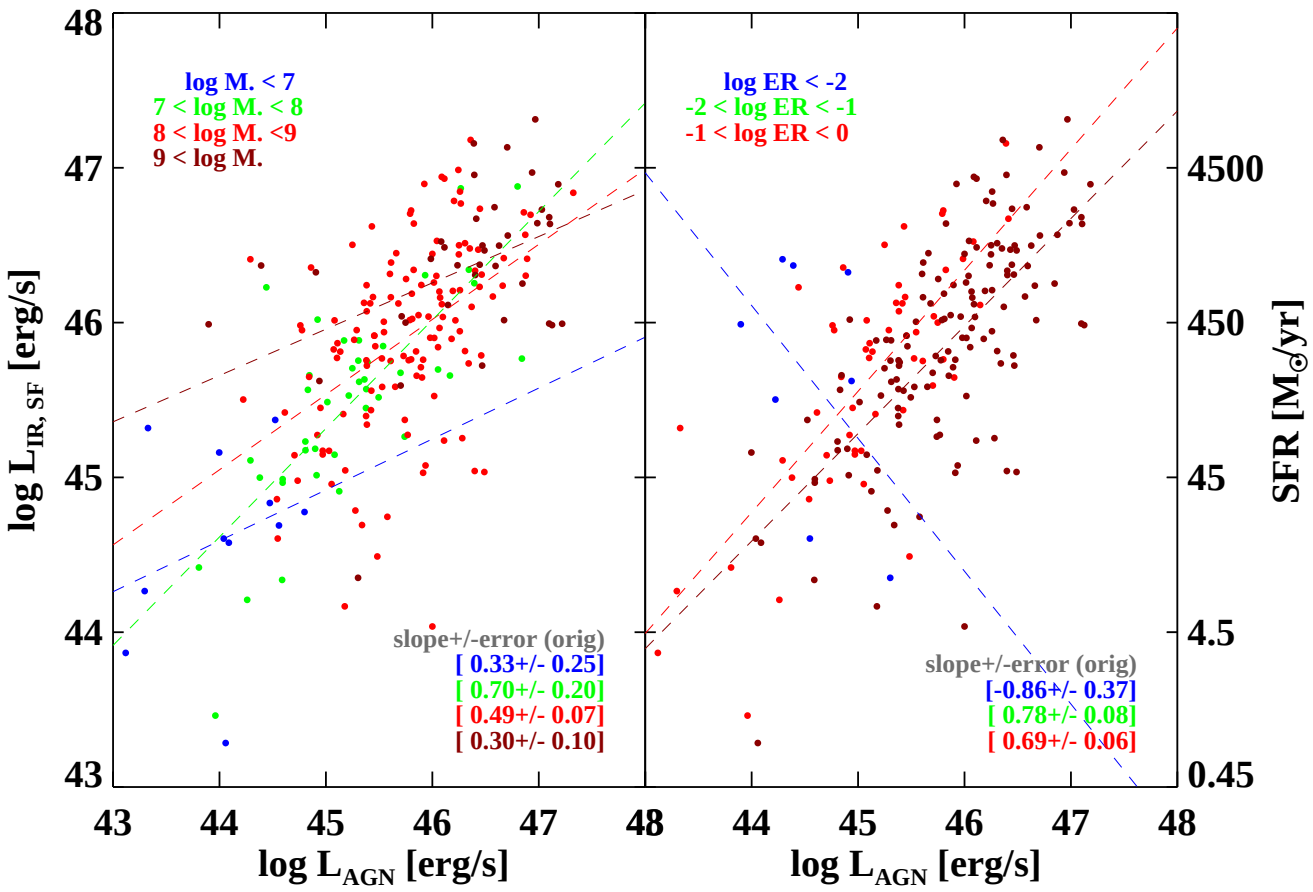

FIG. 4.— Same as Figure 5 but binned by SMBH mass ($M_\bullet$,left) and Eddington ratios (ERs, right). The fitted power-law slopes are based on individual data points in each bin. Positive linear correlations are found between L_X and $L_{IR,SF}$ across different ER and BH masses except at low ER (log ER < -2) due to small number statistics.

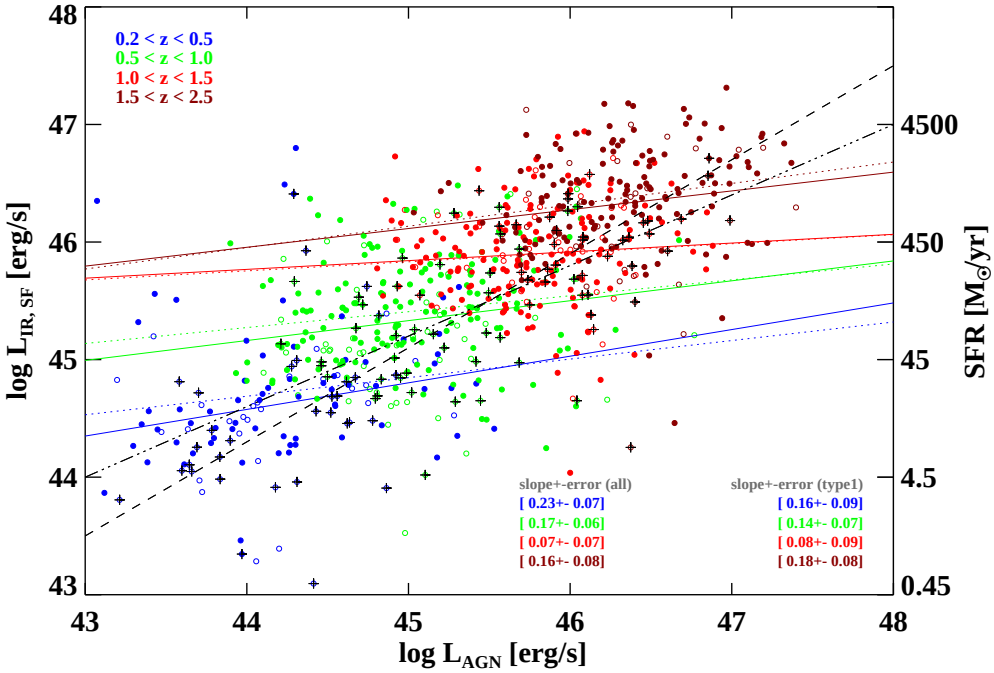

FIG. 5.— Correlation between $L_{\rm AGN}$ and the AGN removed $L_{\rm IR,SF}$ for the IR-bright AGN sample, color coded by redshift. The filled (open) circles are the same as in Figure. 1. Objects detected in hard band only (X-ray lower limits) are marked with a cross. The dash-dotted line is the correlation for the full sample without binning, as in Figure 3. The solid lines are the linear fit to the data in each redshift bin, and the dotted lines are the same fit for type 1 AGNs only. The dash line marks the normalized Netzer (2009) relation implied from local type 2 AGNs. Weak positive correlations are observed between $L_{\rm AGN}$ and $L_{\rm IR,SF}$, in $z < 1.0$, where at $z > 1.0$ the correlation is not significant for the full AGN sample, including both type 1 and type 2 objects. The fitted linear slopes are consistent between different redshift bins except in $1.0 < z < 1.5$, and among type 1 objects.

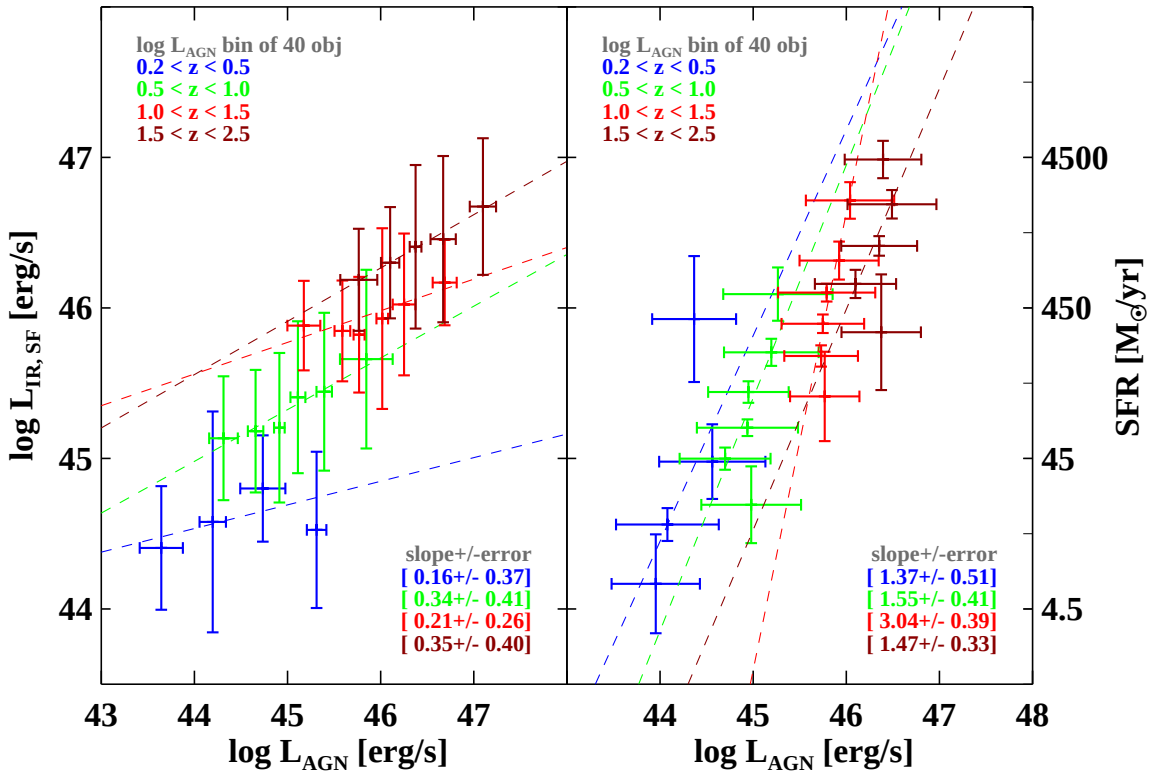

FIG. 6.— Averaged IR luminosity of the IR-bright AGNs binned by $L_{\rm AGN}$ (left) and $L_{\rm IR,SF}$(right), color coded by redshift. The error bars represents the standard deviation in the corresponding luminosity ranges. Binning the data by $L_{\rm IR,SF}$ results in steeper correlations, consistent with the shorter AGN variability timescale.

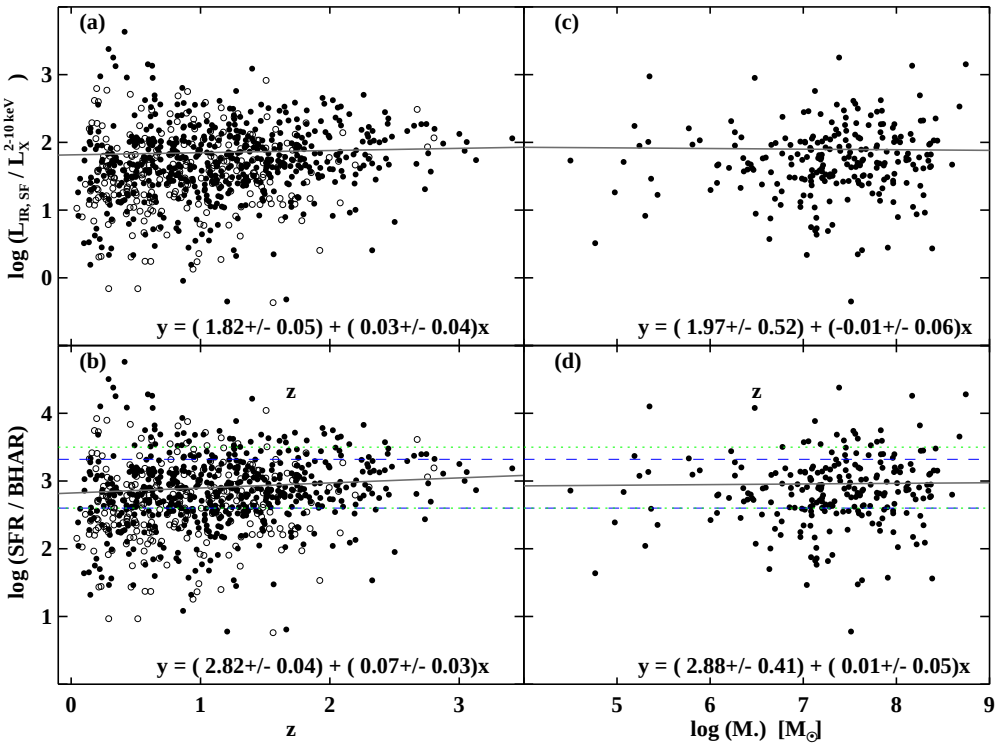

FIG. 7.— The ratios between redshift (left) and SMBH mass (right) and (*Top*) AGN-removed $L_{\rm IR,SF}$ and hard X-ray luminosity $L_{\rm X}$, and (*bottom*) SFR and BHAR. Filled and open circles mark the unobscured type 1 and obscured type 2 objects. The solid lines are the linear fits to the full IR-bright AGN sample, with the fitted function marked in each panel. We observe a constant ratio of ~ 1.82 for the luminosity ratios ($L_{\rm IR,SF}/L_{\rm X}$) and ~ 2.82 for the mass formation/accretion ratios (SFR/BHAR). The intrinsic scatter (standard deviation) is 0.57 in the left panel and 0.55 for the right panel, where only type 1 AGNs with $\rm M_\bullet$ estimate are included. Inclusion of the $z < 0.2$ and $2.5 < z < 4.2$ supplement sample yields consistent results. In the bottom panels, the dashed blue lines mark the range of the $M_*/\rm M_\bullet$ ratios from Marconi & Hunt (2003), and the dotted green lines mark the range in Merritt & Ferrarese (2001); McLure & Dunlop (2002), which reported the same values. The slightly increasing slopes in panel (a) and (b) are due to the selection bias of more luminous objects at high z. Since BHAR is not affected by the FIR flux limits, any undetected IR-bright AGNs would populate the lower SFR/BHAR region at high z, flattening the slope.